CRYSTALLOGRAPHY REPORTS, 2025, Vol. 70, No. 1, pp. 18–26

LATTICE DYNAMICS AND PHASE TRANSITIONS

DYNAMICS OF NEW PHASE FORMATION IN SILICON DURING FEMTOSECOND LASER ABLATION

© 2025 E. I. Mareev[a,*], D. N. Khmelenin[a], and F. V. Potemkin[b]

[a] *Shubnikov Institute of Crystallography, Kurchatov Complex of Crystallography and Photonics, National Research Centre "Kurchatov Institute", Moscow, Russia*

[b] *Lomonosov Moscow State University, Moscow, Russia*

**e-mail: mareev.evgeniy@physics.msu.ru*

Received November 21, 2024
Revised November 21, 2024
Accepted November 25, 2024

Abstract. We experimentally demonstrated (using micro-Raman spectroscopy and transmission electron microscopy) and through numerical simulation that under intense (10^{13} – 10^{14} W/cm^2) femtosecond (~100 fs) laser pulse impact the surface of silicon with (111) orientation, new polymorphic phases Si-III and Si-XII are formed both on the surface and inside the volume, localized in lattice defects as well as at the periphery of the ablation crater. This localization of phases is caused by the multi-stage nature of laser-induced phase transitions in silicon, specifically, the phase transitions are initiated by a shock wave, resulting in a cascading transformation process on sub-nanosecond timescales: Si-I => Si-II => Si-III/Si-XII. The phase transition Si-I => Si-II occurs at the front of the shock wave, while at the rear of the shock wave, a field of dynamic stresses arises in the material, allowing the phase transition Si-II => Si-III/Si-XII to occur. On sub-microsecond timescales, most of the new phases disappear as the material relaxes back to its original state.

DOI: 10.31857/S00234761250103e4

INTRODUCTION

Silicon is one of the most important elements for modern microelectronics. Under normal conditions, silicon has a cubic diamond lattice structure (Si-I) [1]. However, Si-I silicon is an indirect bandgap semiconductor, which complicates its application in optoelectronics, for example, in the development of light-emitting diodes [2]. One possible solution to this problem is the use of Si-I polymorphs, of which more than a dozen variants currently exist [3, 4]. However, under normal conditions, most polymorphic phases are unstable. Transitions to polymorphic phases in silicon occur under high pressure. Additionally, some polymorphic phases, such as Si-III, Si-IV, and Si-XII, are extremely temperature-sensitive and degrade when heated by more than 40 K [2]. At room temperature, silicon retains its cubic crystal lattice up to 11.7 GPa [5]; under dynamic loading, such as that generated by laser-induced shock waves, phase transitions can occur at lower pressures [4]. At pressures above 11.7 GPa, Si-I transitions to the metallic β-tin phase (Si-II) [6, 7]. The pressure range in which the β-tin phase is stable is narrow, and when the pressure exceeds 15 GPa, a sequential chain of phase transitions occurs: β-tin → *Imma* (Si-XI) at 15 GPa → **HCP** – hexagonal close-packed at 42 GPa (Si-V) → **FCC** – face-centered cubic at 78 GPa (Si-VII) [8]. Moreover, another possible chain of phase transitions exists. If the pressure rapidly decreases after the transition to the β-tin phase, a transition to the Si-IX phase becomes possible. With slow changes in pressure, transitions to Si-XII, Si-III, and Si-IV phases can occur [2]. These last three polymorphs are metastable at atmospheric pressure. These phases have been detected in diamond anvil cell experiments using Raman spectroscopy, as new peaks appeared in the Si spectrum [9–11]. The use of short (nanosecond) and ultrashort (pico- and femtosecond) laser pulses is an alternative method for generating high pressure and studying new material phases [12]. Due to the high intensities achieved when focusing laser radiation, it becomes possible to reach pressures in samples up to terapascal levels, opening opportunities for studying entirely new material phases [13]. A distinctive feature of this approach is the pulsed impact on the material, which allows the initiation of ultrafast (up to several femtoseconds) phase transitions. Furthermore, depending on the duration and energy of the laser pulse, unique pressure-temperature profiles can be created: for instance, femtosecond laser impact causes localized heating in a solid, while nanosecond exposure results in nearly an order of magnitude higher medium heating. The pressures achieved in both cases are comparable [14, 15]. Thus, by varying the parameters of laser impact, unique conditions for phase transitions can be achieved. With the development of megascience-class

facilities, such as free-electron lasers and synchrotron radiation sources, the study of the dynamics of phase transitions initiated by short and ultrashort laser pulses has reached a new level [4, 16–19]. However, with direct laser impact on the semiconductor surface, in addition to the generation of high pressures (primarily at the shock wave front), crystal lattice heating, ablation, and shock wave generation also occures [20, 21], significantly complicating the dynamics of the processes involved.

To fully control the dynamics of phase transitions in silicon, it is essential to completely understand the nature of the ongoing processes. One of the most effective tools for studying fast processes in the crystal lattice is numerical simulation, which can fully reconstruct its dynamics at the atomic level [22]. For simulation laser-induced processes in solids, molecular dynamics (**MD**) combined with the two-temperature model (**TTM**) can be used: MD + TTM [23–29]. In this approach, the laser pulse interacts with the electronic subsystem, rapidly heating it, while the atomic subsystem is not directly affected—the energy is transferred from the electronic to the atomic subsystem; the atomic subsystem is modeled using classical MD [23–29]. Nevertheless, any theoretical model must be verified. Since reconstructing the dynamics of laser exposure is extremely challenging, the model was verified using post-mortem diagnostics, specifically through surface analysis using micro-Raman spectroscopy and transmission electron microscopy (**TEM**).

METHODS AND MATERIALS

Silicon samples (silicon substrates (111)) were uniformly exposed to femtosecond radiation from a chromium-forsterite laser system, with a 10 μm spacing between craters (repetition rate of 10 Hz, energy of 10 μJ, wavelength of 1240 nm, focused using a lens with a numerical aperture of 0.5). The sample was moved using a motorized linear translator with a step size of 1 μm. The laser pulse impact on the surface resulted in the formation of microcraters approximately 10 μm in diameter. For comparison with femtosecond exposure, radiation from a nanosecond laser system, Quantel Rio, was also used (energy up to 100 mJ, pulse duration of 4 ns, wavelength of 1064 nm). After laser impact, the sample was analyzed using Raman microspectroscopy (Fig. 1). Measurements were performed using a Nicolet Almega XR spectrometer with a 532 nm laser excitation source (continuous Nd:YAG laser generating a second harmonic with a power of 20 mW). The spectrometer was equipped with a microscope fitted with 10×, 50×, and 100× objectives. During microscopic investigations, the laser spot diameter was 1 μm. The Stokes shift components were analyzed in the frequency range of 250–475 cm^{-1} with a spectral resolution of 2 cm^{-1}. The monochromator was calibrated using the characteristic silicon peak at 521 cm^{-1}. The obtained spectra were processed using OMNIK software. Additionally, the sample surface was examined using TEM and electron diffraction methods with an FEI Tecnai Osiris microscope (ThermoFisher Scientific, USA) featuring a point resolution of 2.5 Å and a line resolution of 1.02 Å at an accelerating voltage of 200 kV (Fig. 2). Cross-sections for TEM analysis were prepared using the lift-out method with a focused ion beam in an FEI Scios dual-beam electron-ion microscope (ThermoFisher Scientific, USA). DigitalMicrograph software (Gatan, USA) was used for image and electronogram processing and analysis.

For numerical simulation of the plasma-material interaction system's evolution, the classical MD software package LAMMPS [30] and the two-temperature model (TTM) [23, 31] were used to describe the interaction of laser radiation with the electronic subsystem and both the electronic and atomic subsystems. The electronic subsystem was modeled as an electron gas, assuming the laser pulse heated the electron gas to temperatures around 10^4 K [14]. Energy transfer to the crystal lattice atoms occurs through both electronic interactions within the electronic subsystem and electron-phonon interactions, described by the equation:

$$C_e \frac{\partial T_e}{\partial t} = \nabla\left(\kappa_e \nabla T_e\right) - g_p\left(T_e - T_a\right) + g_s T_a \,,$$

where T_e and T_a represent the temperatures of the electronic and atomic subsystems, respectively; κ_e is the thermal conductivity coefficient; g_p and g_s are

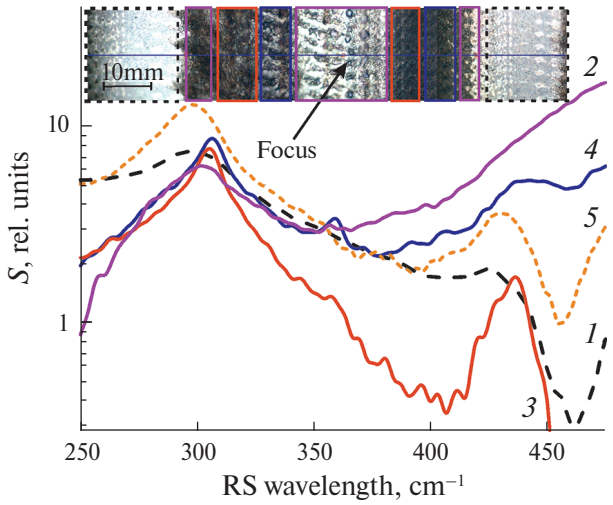

Fig. 1. Image of the region of action of the laser pulse on silicon, as well as Raman spectra in the frequency range of 250–475 cm^{-1}: *1* – spectrum of undamaged silicon, *2* – spectrum of amorphous silicon, *3* – region where the peak characteristic of the Si-III phase at 430 cm^{-1} is recorded in the spectra, *4* – spectrum containing peaks of the Si-III and Si-XII phases, *5* – spectrum with nanosecond laser action on silicon. Rectangles in the microscopic image indicate the regions in which the corresponding spectra are measured.

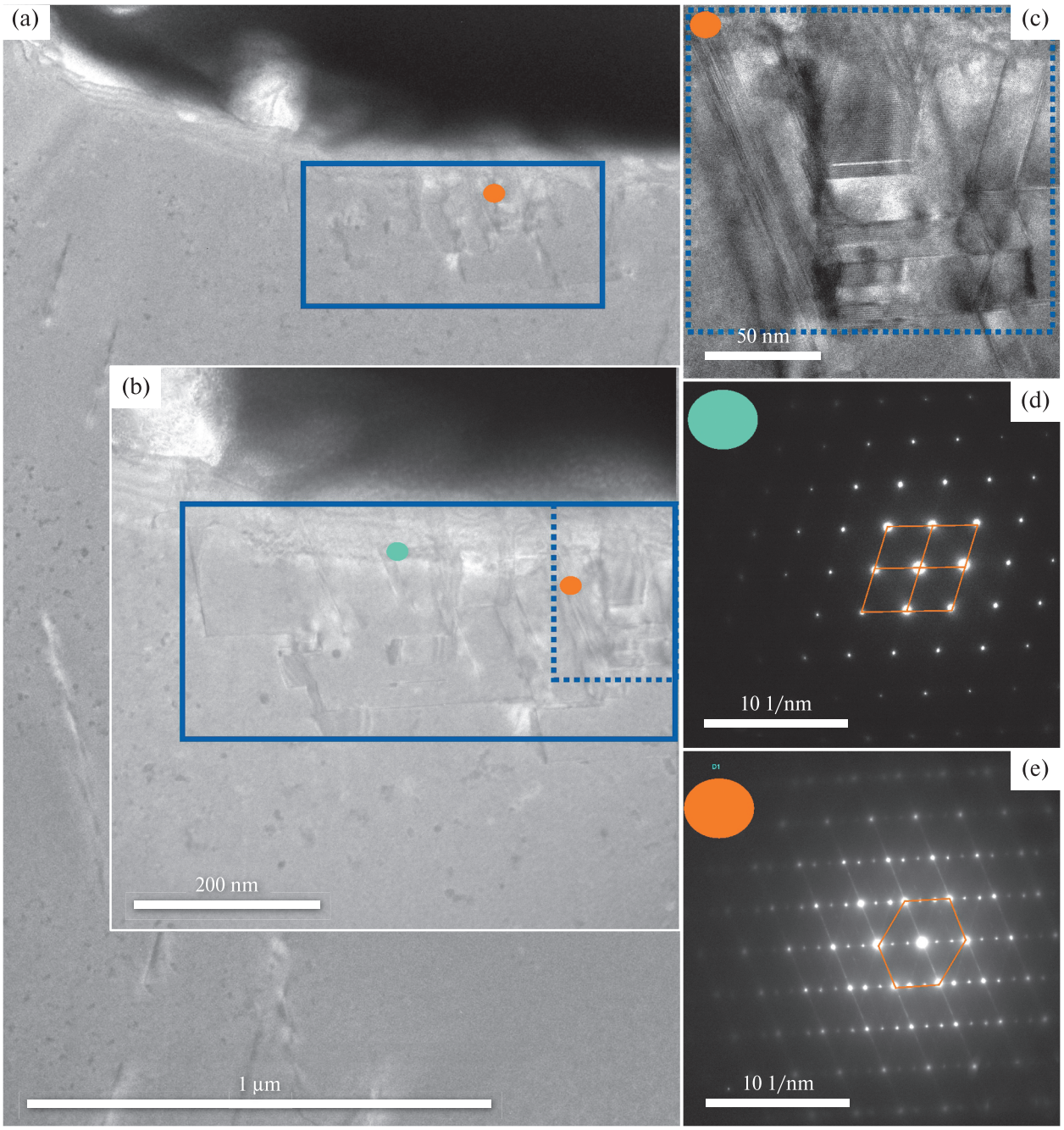

Fig. 2. TEM images of the laser-induced microcrater region: a – general view, dark areas on top are typical for amorphous silicon, oblique lines in the figures are lattice dislocations; b, c – enlarged areas marked with rectangles in Fig. a; d, e – electron diffraction patterns from areas marked with dots.

interaction constants; and Ce is the electronic heat capacity, linearly dependent on the electron temperature [32]. The full system model is described in [25], and the numerical values of the parameters used in the model are presented in Table 1. It was assumed that the laser pulse duration is much shorter than the characteristic times of phase transitions, meaning laser impact affects only the initial profile (concentration and temperature of plasma electrons), corresponding to the results obtained in [14]. The laser waist diameter (the distance from the axis where intensity drops by a factor of e^2) was set to 44 Å, and the Rayleigh length (along the laser pulse propagation axis) was 150 Å. The simulation area size was 440 × 440 × 1550 Å, with the laser pulse propagating along the z-axis. The laser-affected region's parameters were proportional to the actual waist dimensions but

Table 1. Simulation parameters used to calculate femtosecond laser ablation of silicon

Variable	Units of measurement	Value
a_0	$eV \cdot K^{-1}$	0.005
r_{emax}	N_{at}	0.16
D_e	$Å^2 \cdot ps^{-1}$	32.436
g_p	$g \cdot mole^{-1} \cdot ps^{-1}$	11.235
g_s	$g \cdot mole^{-1} \cdot ps^{-1}$	8.443
V_0	$Å \cdot ps^{-1}$	79.76
I_0	$eV \cdot ps^{-1} \cdot Å^{-2}$	0
$L_{surface}$		0
$R_{surface}$		40
L_{skin}	Å	2
t	ps	0.1
B		60
l	Å	2
N_{ion}	$Å^{-3}$	0.05

approximately 10,000 times smaller. The temperature of the lateral surfaces (not impacted by the laser pulse) was fixed at the initial 300 K. Periodic boundary conditions were not used. The Tersoff potential [32] was employed for simulation interatomic interactions. Calculations were performed with a time step of 0.1 fs up to 300 ps. Before the main simulation cycle, the system was brought to thermodynamic equilibrium for 1 ps, after which the laser interaction with the system was modeled. Results were saved every 1000 steps.

The simulation output included data on the velocity and position of each silicon atom. The Ovito software package [33] was used for data visualization. The analysis involved calculating the specific volume occupied by each atom (atomic volume). Fig. 3 shows the profile of the simulation area along the z-axis (10 Å thick layer), with the color representing the volume of each atom (ranging from 14 to 25 $Å^{-3}$). Fig. 4 displays the distribution of the number of atoms with a given volume. Additionally, for phase transition analysis, rocking curves were calculated on the reciprocal lattice grid defined for the entire simulation area, for X-ray radiation with an energy of 12 keV, similar to the method in [34].

RESULTS

When focusing a femtosecond (100 fs) laser pulse with an energy of about 10 μJ at a wavelength of 1240 nm onto a silicon surface (numerical aperture 0.5), intensities of approximately 10^{13}–10^{14} W/cm^2 and energy densities of ~1 J/cm^2 are achieved, leading to the process of laser ablation, accompanied by the generation of shock waves, the formation of micro-modifications, and a cascade of phase transitions [35]. This study focuses on the analysis of post-mortem phase formation and the development of a numerical model to investigate the dynamics of this process. Laser impact on the silicon surface using a femtosecond laser in a pulse-periodic mode was performed such that the boundaries of the microcraters created by the laser pulses were adjacent, forming a quasi-homogeneous modified region of 10 × 10 μm. Microcrater analysis was then performed using micro-Raman spectroscopy, with comparisons made to nanosecond laser impact. In the center of the crater (Fig. 1), there is an amorphous silicon region, surrounded by an area where peaks characteristic of the Si-III phase (430 cm^{-1}) [36] are observed, followed by an area in which, in addition to Si-III, a peak characteristic of Si-XII (353 cm^{-1}) [36] is also present. The periphery contains a region of unmodified silicon with nanoparticles formed as a result of mass ejection during the laser ablation process. Thus, it can be noted that at the center of the crater, only amorphous silicon is observed, while polymorphic phases are found in small quantities at the periphery of the crater.

Microcraters were also diagnosed using SEM, and the main results are presented in Fig. 2. For ion beam studies, a subsurface region was sectioned. The SEM shows that the structure of the microcrater consists of an upper amorphous layer, followed by a crystalline silicon region where sequences of banding shifts are observed. The closer to the crater center, the more deformations are observed. The expansion direction of these planar defects is slightly tilted from [112] by approximately 7°. Thus, the planar defect may be associated with stacking faults [37]. The average width of the defects is less than 10 nm, and they are distributed over just a few atomic layers. Additionally, areas of shear deformation and the undamaged volume of silicon were investigated using electron diffraction. The analysis shows that, except for the material in the shear deformation zone, the silicon structure is similar to the original one, i.e., polymorphic phases are registered only in the "traps" formed during the creation of shear deformations. Electron diffraction patterns show a cubic diamond lattice type (Fig. 2d) [38]. However, in the shear deformation zone, the Si-III phase is present according to electron diffraction (Fig. 2d) [39]. Numerical simulation allows a better understanding of both the dynamics of new phase formation and why new polymorphic phases are observed only in small amounts at the periphery of laser exposure in post-mortem analysis, as shown experimentally.

The MD simulations can vividly demonstrate the dynamics of new phase formation in the microcrater. To analyze phase transitions, the laser-induced dynamic behavior was visualized by color indicating specific atomic

volume. Since the crystal lattice changes during phase transitions, resulting in a change in the specific volume occupied by each atom, this parameter can serve as a criterion for phase transition. At the initial stages of laser ablation, the density decreases, and atomic bonds break in the region directly affected by the laser (Fig. 3, 1 ps), resulting in a compression of silicon by 30-40%. This leads to the generation of a shock wave, which forms approximately 3-4 ps after laser impact (Fig. 3). At the shock wave's leading edge, the atomic distance decreases

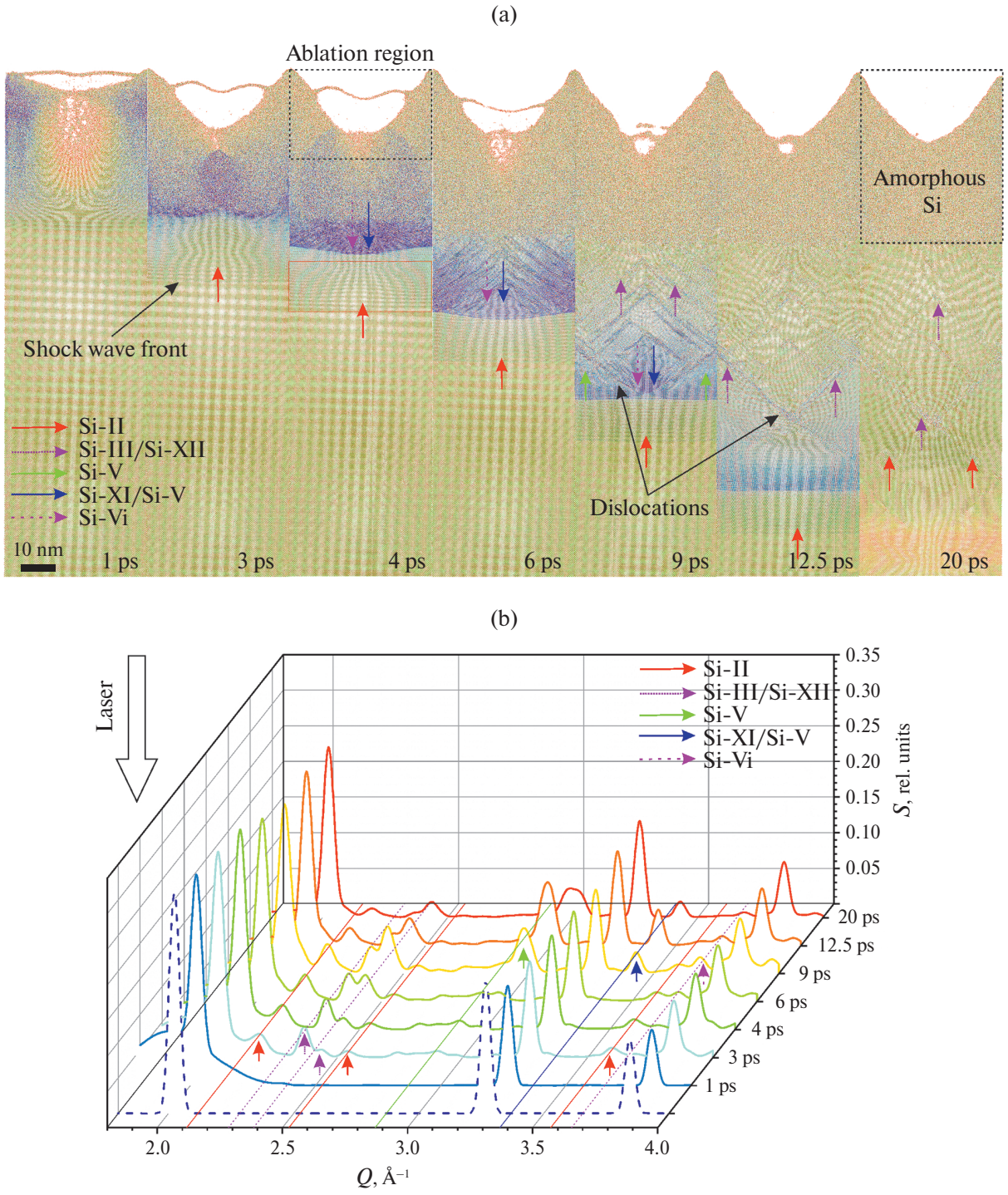

Fig. 3. Visualization of the numerical simulation results – a cross-section of a 10 Å thick silicon sample along the laser pulse propagation axis (from left to right) (a): the brightness shows the atomic volume of the Si-I phases, compressed Si-I, Si-II and Si-XI, Si-III and Si-XII, and regions with lower density. The time delay for each image is indicated in the figure. Evolution of the dynamics of the rocking curve calculated for the near-surface region (b): the arrows indicate the peaks and atomic volumes characteristic of silicon phases other than Si-I.

due to high pressure (50 GPa), leading to a reduction in atomic volume and a shift in the center of mass of its distribution histogram (Fig. 4). At the shock wave's rear edge, a transition to the Si-II phase occurs, as evidenced by the appearance of a histogram peak representing 0.75 of the original atomic volume, as well as additional peaks in the diffraction patterns (Fig. 3), which correlate well with results from [40]. This atomic volume (0.75 of the original) is characteristic of this phase [41]. Due to energy loss from the shock wave, pressure and lattice compression decrease, resulting in rarefaction, and peaks characteristic of compressed silicon and Si-II shift towards larger atomic volumes over time. During this period, at the rear edge, a jump in atomic volume occurs due to the relatively slow pressure decrease (700 MN/s) at around 12.5 ps, characterizing the transition to the Si-III/Si-XII phase, which is also accompanied by new diffraction peaks corresponding to data from [42]. Because these phases have similar atomic volumes and diffraction patterns, they are difficult to distinguish from one another [43, 44]. In Fig. 3, the formation of these phases is noticeable in the region located between the shock wave front and the amorphous material near the crater. The figure also clearly shows areas of shear deformation occurring behind the shock wave front, which are similar to those observed in the SEM, with the directions of deformation formation fully matching the experimental data. When the system reaches equilibrium, these areas become less noticeable but do not completely disappear — it is within these areas that remnants of the Si-III/Si-XII phases remain, which vanish in the rest of the material (except for the amorphous layer). As a result, the final silicon structure after laser impact is formed: a crater mostly composed of amorphous silicon; a region containing shear deformations; and, deeper, a structure close to the original material.

In addition to shock wave generation, laser impact leads to lattice heating. Although the initial temperature of the atomic subsystem is room temperature, rapid heating to ~2000 K occurs in the laser-affected region (Fig. 3, 1 ps) due to heat transfer from the electronic subsystem to the atomic subsystem over timescales of about 1 ps, with the rest of the lattice remaining unheated. This rapid heating leads to almost complete lattice destruction in this region. Due to thermal diffusion, heat begins to spread, but at much slower speeds than the shock wave (~10 km/s). After about 10 ps, the lattice is heated by ~100 K.

DISCUSSION

The combination of numerical simulation with *post-mortem* diagnostics give opportunity to determine the origin of the characteristic pattern of polymorphic silicon phase formation after laser impact. Only the Si-III/Si-XII phases are experimentally observed, which also corresponds to diffraction experiments [35]. The quantity of these phases is small, and, as micro-Raman spectroscopy shows, these phases are located at the periphery of the ablation crater. The crater itself primarily consists of amorphous silicon. Within the volume, new polymorphic phases are also localized in shear deformations, not distributed throughout the entire volume. Thus, the generation of high pressures alone [22] does not guarantee that the polymorphic phases will be stable; the achieved temperature and rate of pressure reduction play a key role. Therefore, the regimes of laser impact themselves determine the features of new phase formation.

Let us now consider the dynamics of laser impact on a semiconductor. When the laser pulse is focused on the semiconductor surface, an electron plasma is generated, which absorbs the energy of the laser pulse. The electrons begin transferring energy to the atoms [14]. As a result, the following temperature distribution is realized at this stage: hot electrons with a

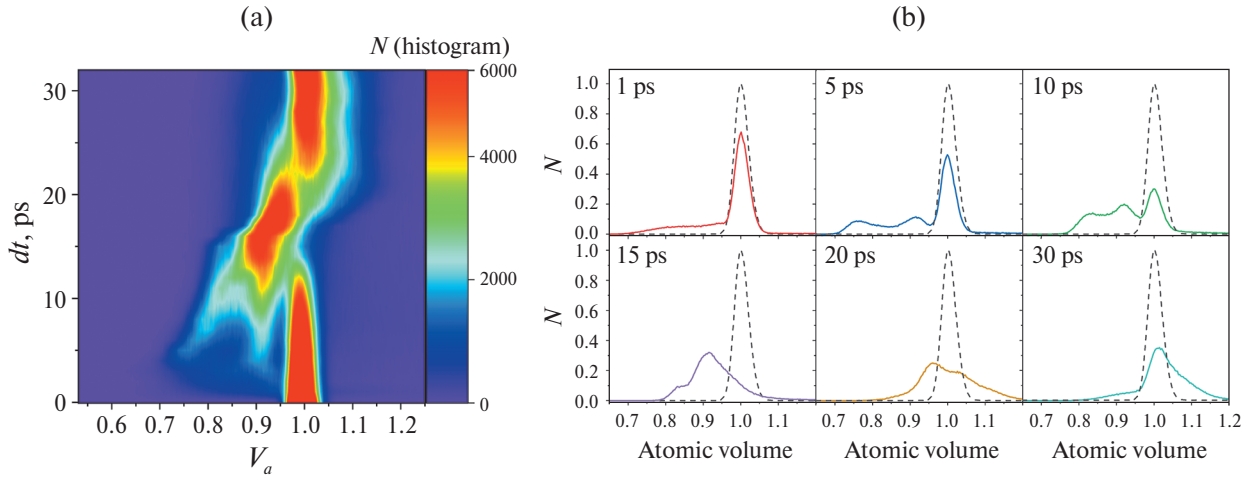

Fig. 4. Time dynamics of changes in the histogram of atomic volume distribution after laser exposure: a – three-dimensional heat map, b – histograms of atomic volume distribution for times of 2, 5, 10, 15, 20, 30 ps. The dashed line indicates the original histogram.

temperature of ~10^4 K and cold ions at ~300 K, which is used in the model. Due to energy transfer from the electron subsystem to the atomic subsystem, a shock wave is generated, which begins to propagate from the impact zone and displace atoms from their equilibrium positions, with the amplitude of this displacement being about 1 Å, which is comparable to interatomic distances. Furthermore, the lattice also begins to heat up, with the near-surface region heating to thousands of kelvins. This leads to the destruction of the crystal lattice directly in the affected area (Fig. 5). The further heat propagation from the affected zone is determined by thermodiffusion and is a relatively slow process. The shock wave continues its propagation, and the displacement of atoms may reach values comparable to interatomic distances. This leads to strong anharmonicity of the processes, causing an atom to "forget" the original structure of the substance it was in. Since its neighbors are also in similar conditions, and the pressure is tens of gigapascals, all the conditions for phase transitions are created. The first phase transition Si-I → Si-II occurs at the rear front of the shock wave within timescales of 1–5 ps. The Si-II phase is unstable, and as the pressure decreases, a transition to the Si-III and Si-XII phases occurs. It is also possible that this phase transition is realized through another metastable phase Si-XI [2]. Defect formation is one of the efficient ways to relieve the stresses that arise from the application of external pressure and deformation of silicon [37]. The direction of defect formation deviates by approximately 7° from the [112] axis. At the initial stage of shock wave propagation (pressures below 11 GPa), defect formation is the preferred method of relieving the stress in the lattice. When the pressure caused by the shock waves exceeds 11 GPa, the metallic Si-II phase forms, and additional stress is easily relieved through phase transitions and deformation of Si-II. Local stress should be the primary factor for defect formation, and this process may also be further enhanced by temperature increases of several hundred degrees due to the laser exposure. One possible mechanism for defect formation is as follows [37]: defects form through complete dislocation of layers, which is triggered to reduce the local high stress around the point of stress concentration caused by the passage of shock waves and phase transitions. However, after the shock wave passes, high temperatures reach the area where the Si-III and Si-XII phases formed, leading to the annealing of the formed phase and a return to the original Si-I phase [2, 10]. Therefore, post-mortem diagnostics only manage to register those phases that were not subjected to thermal impact. Increasing the energy of the laser pulse will lead to an increase in pressure, which may initiate transitions to the Si-VI, Si-XII phases [2]. However, this will not form new phases that are stable at atmospheric pressure. It will also lead to additional heating of the material and destruction of new phases. Similarly, increasing the duration of the laser pulse will lead to a rise in temperature, which is confirmed by the results of studying nanosecond exposure on the silicon surface, where a greater amount of amorphous silicon is observed with virtually no new phases.

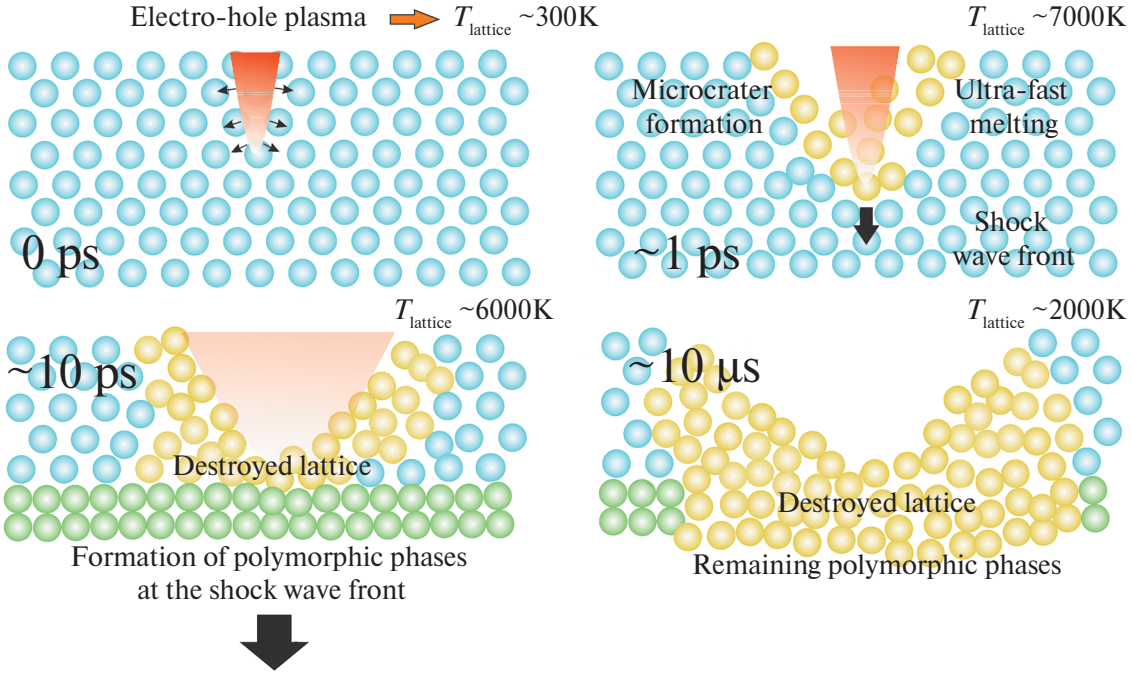

Fig. 5. Schematic representation of the dynamics of laser-induced phase transitions in silicon.

CONCLUSION

A numerical approach based on molecular dynamics in combination with a two-temperature model has been developed, which qualitatively predicts the dynamics of structural transformations in silicon subjected to intense femtosecond laser exposure. The final structure is a microcrater, at the base of which (surface and near-surface regions) amorphous silicon is present. At the periphery of the crater, as well as in the volume in areas of shear deformation, inclusions of Si-III and Si-XII phases form. These phases are generated through a cascade of phase transitions Si-I → Si-II → Si-XI → Si-III/Si-XII. The laser-induced shock wave (pressures at the front ~50 GPa) primarily initiates phase transitions. Shock waves displace atoms in the lattice by more than 1 Å, which leads to stresses in the lattice and, as a result, either the formation of shear deformations or phase transitions. Phase transitions occur behind the shock wave front, and subsequent laser-induced heating of the lattice (~2000 K directly in the laser impact area and ~100 K in the majority of the remaining material) leads to the destruction of residual metastable Si-III/Si-XII phases, which remain only in areas where the heating was lower (periphery) or where residual stresses persisted.

FUNDING

The work was supported by the Russian Science Foundation (grant No. 23-73-00039) in terms of molecular dynamics and Raman microspectroscopy, as well as within the framework of the state assignment of the National Research Center "Kurchatov Institute" in terms of studying silicon by electron microscopy methods using the equipment of the Collective Use Center "Structural Diagnostics of Materials" of the Kurchatov Crystallography and Photonics Complex of the National Research Center "Kurchatov Institute".

REFERENCES

1. *Mogni G., Higginbotham A., Gaál-Nagy K., Park N., Wark J.S.* // Phys. Rev. B. 2014. V. 89. P. 064104. https://doi.org/10.1103/PhysRevB.89.064104
2. *Wippermann S., He Y., Vörös M., Galli G.* // Appl. Phys. Rev. 2016. V. 3. P. 040807. https://doi.org/10.1063/1.4961724
3. *Hanfland M., Schwarz U., Syassen K., Takemura K.* // Phys. Rev. Lett. 1999. V. 82. P. 1197. https://doi.org/10.1103/PhysRevLett.82.1197
4. *McBride E.E., Krygier A., Ehnes A. et al.* // Nat. Phys. 2019. V. 15. P. 89. https://doi.org/10.1038/s41567-018-0290-x
5. *Mareev E.I., Rumyantsev B.V., Potemkin F.V.* // Letters to JETP. 2020. V. 112. P. 780. https://doi.org/10.31857/s1234567820230111
6. *Budnitzki M., Kuna M.* // J. Mechan. Phys. Solids. 2016. V. 95. P. 64. https://doi.org/10.1016/j.jmps.2016.03.017
7. *Chen H., Levitas V.I., Popov D., Velisavljevic N.* // Nat. Commun. 2022. V. 13. P. 982. https://doi.org/10.1038/s41467-022-28604-1
8. *Daisenberger D., Wilson M., McMillan P.F. et al.* // Phys. Rev. B. 2007. V 75. P. 224118. https://doi.org/10.1103/PhysRevB.75.224118
9. *Domnich V., Gogotsi Y.* // Rev. Adv. Mater. Sci. 2002. V. 3. P. 1. https://www.ipme.ru/e-journals/RAMS/no_1302/domnich/domnich.pdf
10. *Zeng Z., Zeng Q., Mao W.L., Qu S.* // J. Appl. Phys. 2014. V. 115. P. 103514. https://doi.org/10.1063/1.4868156
11. *Ovsyuk N.N., Lyapin S.G.* // Appl. Phys. Lett. 2020. V. 116. P. 062103. https://doi.org/10.1063/1.5145246
12. *Sundaram S.K., Mazur E.* // Nat. Mater. 2002. V. 1. P. 217. https://doi.org/10.1038/nmat767
13. *Vailionis A., Gamaly E.G., Mizeikis V. et al.* // Nat. Commun. 2011. V. 2. P. 445. https://doi.org/10.1038/ncomms1449
14. *Mareev E.I., Lvov K.V., Rumiantsev B.V. et al.* // Laser Phys. Lett. 2019. V. 17. P. 015402. https://doi.org/10.1088/1612-202X/ab5d23
15. *Butkus S.* // J. Laser Micro/Nanoengineering. 2014. V. 9. P. 213. https://doi.org/10.2961/jlmn.2014.03.0006
16. *Gorman M.G., Briggs R., McBride E.E. et al.* // Phys. Rev. Lett. 2015. V. 115. P. 095701. https://doi.org/10.1103/PhysRevLett.115.095701
17. *Brown S.B., Gleason A.E., Galtier E. et al.* // Sci. Adv. 2019. V 5. P. eaau8044. https://doi.org/10.1126/sciadv.aau8044
18. *Potemkin F.V., Mareev E.I., Garmatina A.A. et al.* // Rev. Sci. Instrum. 2021. V. 92. P. 053101. https://doi.org/10.1063/5.0028228
19. *Kovalchuk M.V., Borisov M.M., Garmatina A.A. et al.* // Crystallography. 2022. V. 67. No. 5. P. 771. https://doi.org/10.31857/s0023476122050083
20. *Moser R., Domke M., Winter J. et al.* // Adv. Opt. Technol. 2018. V. 7. P. 255. https://doi.org/10.1515/aot-2018-0013
21. *Mareev E., Obydennov N., Potemkin F.* // Photonics. 2023. V. 10. P. 380. https://doi.org/10.3390/photonics10040380.
22. *Mareev E.I., Potemkin F.V.* // Int. J. Mol. Sci. 2022. V. 23. P. 2115. https://doi.org/10.3390/ijms23042115
23. *Norman G.E., Starikov S.V., Stegailov V.V.* // JETP. 2012. V. 141. P. 910. https://doi.org/10.1134/S1063776112040115
24. *Greathouse J.A.* Two-Temperature (TTM) Molecular Dynamics. Standia National LAborotory, NNSA.

25. *Mareev E., Pushkin A., Migal E. et al.* // Sci. Rep. 2022. V. 12. P. 7517. https://doi.org/10.1038/s41598-022-11501-4
26. *Yang J., Zhang D., Wei J. et al.* // Micromachines. 2022. V. 13. P. 1119. https://doi.org/10.3390/mi13071119
27. *Taylor L.L., Scott R.E., Qiao J.* // Opt. Mater. Express. 2018. V 8. P. 648. https://doi.org/10.1364/ome.8.000648
28. *Liu J., Wu M., Sun Z. et al.* // Appl. Surf. Sci. 2024. V. 661. P. 160022. https://doi.org/10.1016/j.apsusc.2024.160022
29. *An H., Wang J., Fang F., Jiang J.* // Opt. Laser Technol. 2024. V. 171. P. 110427. https://doi.org/10.1016/j.optlastec.2023.110427
30. *Plimpton S.* // J. Comput. Phys. 1995. V. 117. P. 1. https://doi.org/10.1006/jcph.1995.1039
31. *Pisarev V.V., Starikov S.V.* // J. Phys.: Condens. Matter. 2014. V. 26. No. 47. P. 475401. https://doi.org/10.1088/0953-8984/26/47/475401
32. *Norman G.E., Starikov S.V., Stegailov V.V. et al.* // Contrib. Plasma Phys. 2013. V. 2. P. 129. https://doi.org/10.1002/ctpp.201310025
33. *Stukowski A.* // Model. Simul. Mat. Sci. Eng. 2010. V. 18. No. 1. P. 015012. https://doi.org/10.1088/0965-0393/18/1/015012
34. *Coleman S.P., Spearot D.E., Capolungo L.* // Model. Simul. Mat. Sci. Eng. 2013. V. 21. P. 055020. https://doi.org/10.1088/0965-0393/21/5/055020
35. *Pashaev E.M., Korchuganov V.N., Subbotin I.A. et al.* // Crystallography. 2021. V. 66. P. 877. https://doi.org/10.31857/S0023476122050083
36. *Gogotsi Y., Baek C., Kirscht F.* // Semicond. Sci. Technol. 1999. V 10. P. 936. https://doi.org/10.1088/0268-1242/14/10/310
37. *Li H., Yu X., Zhu X. et al.* // AIP Adv. 2021. V. 4. P. 045103. https://doi.org/10.1063/5.0034896
38. *Bradby J.E., Williams J.S., Wong-Leung J. et al.* // Appl. Phys. Lett. 2000. V. 23. P. 3749. https://doi.org/10.1063/1.1332110
39. *Ikoma Y., Yamasaki T., Shimizu T. et al.* // Mater. Characterization. 2020. V. 169. P. 110590. https://doi.org/10.1016/j.matchar.2020.110590
40. *Xuan Y., Tan L., Cheng B. et al.* // J. Phys. Chem. C. 2020. V. 124. P. 27089. https://doi.org/10.1021/acs.jpcc.0c07686
41. *Cheng C.* // Phys. Rev. B 2003. V. 67. P. 134109. https://doi.org/10.1103/PhysRevB.67.134109
42. *Anzellini S., Wharmby M.T., Miozzi F. et al.* // Sci. Rep. 2019. V. 9. P. 15537. https://doi.org/10.1038/s41598-019-51931-1
43. *Yin M.T.* // Phys. Rev. B. 1984. V. 30. P. 1773. https://doi.org/10.1103/PhysRevB.30.1773
44. *Piltz R.O., MacLean J.R., Clark S.J. et al.* // Phys. Rev. B. 1995. V. 52. P. 4072. https://doi.org/10.1103/PhysRevB.52.4072